Bailey, L.R., et al., 2021, Eocene fault-controlled fluid flow and mineralization in the Paradox Basin, United States: Geology, https://doi.org/10.1130/G49466.1

Supplemental Material

Eocene fault-controlled fluid flow and mineralization in the Paradox Basin

Lydia R. Bailey[1], Jason Kirk[1], Sidney R. Hemming[2], Robert W Krantz[1] and Peter W. Reiners[1]

[1]*Department of Geosciences, University of Arizona, Tucson, AZ 85721, USA*

[2]*Lamont-Doherty Earth Observatory, Columbia University, Palisades, NY 10964, USA*

SAMPLE LOCATIONS

We sampled approximately 1 kg of fault gouge from each location, and approximately 1.5 kg of the Rainbow Rocks Sandstone was collected (Figs. DR1-DR9). In all fault gouge samples, the primary slip surface was sampled. We observed macroscopic foliation of the fault gouge, oriented sub-parallel to the primary slip surface, at the Moab Fault, Courthouse Fault, Lisbon Valley Fault, GTO Fault, and Kane Springs Fault. We sampled the Lisbon Valley and Keystone Faults from the Centennial pit at the active Lisbon Valley Mine with the permission of Lisbon Valley Mining Co. and guidance of Lantz Indergard.

Table DR1: Sandstone and fault-gouge sample locations

Sample	Sample #	Latitude (N)	Longitude (W)	Location	Footwall	Hangingwall
Rainbow Rocks Sandstone	18PRPB14	38.69284°	109.91439°	Upper yellow sandstone of paleo-oil reservoir, sampled 2 meters above grey bitumen-bearing horizon	-	-
Moab Fault	MF001	38.633418°	109.649053°	ExxonMobil Field Safety Training video site	Cutler	Morrison-Salt Wash
Courthouse Fault	MF006	38.709656°	109.739126°	East of Mill Canyon	Entrada-Slick Rock	Morrison-Salt Wash and Tidwell
Keystone Fault	LV007	38.140717°	109.129167°	Upper bench at Lisbon Valley Mine, Centennial Pit	Burro Canyon Fm	Burro Canyon Fm
Lisbon Valley Fault	LV002	38.140188°	109.130824°	Upper bench at Lisbon Valley Mine, Centennial Pit, closer to FW	Navajo Sst	Burro Canyon Fm
GTO Fault	LV012	38.104285°	109.101248°	Trench cut, lower exposure at Lucky Strike	Morrison-Salt Wash	Burro Canyon Fm
Cliffdweller Fault	20LBCM02	38.31242°	108.95381°	Gouge taken from Cliffdweller fault by Maude mine adit	Wingate Sst	Wingate Sst
Salt Valley Fault	MF010	38.858426°	109.742714°	Exposed fault scarp NE side of NW Salt valley, near horse corral	Navajo Sst	Mancos Shale & Ferron Sst
Kane Springs Fault	MF011	38.405985°	109.448062°	West side of Hwy 191, road cut at top of hill	Morrison-Tidwell	Morrison-Tidwell

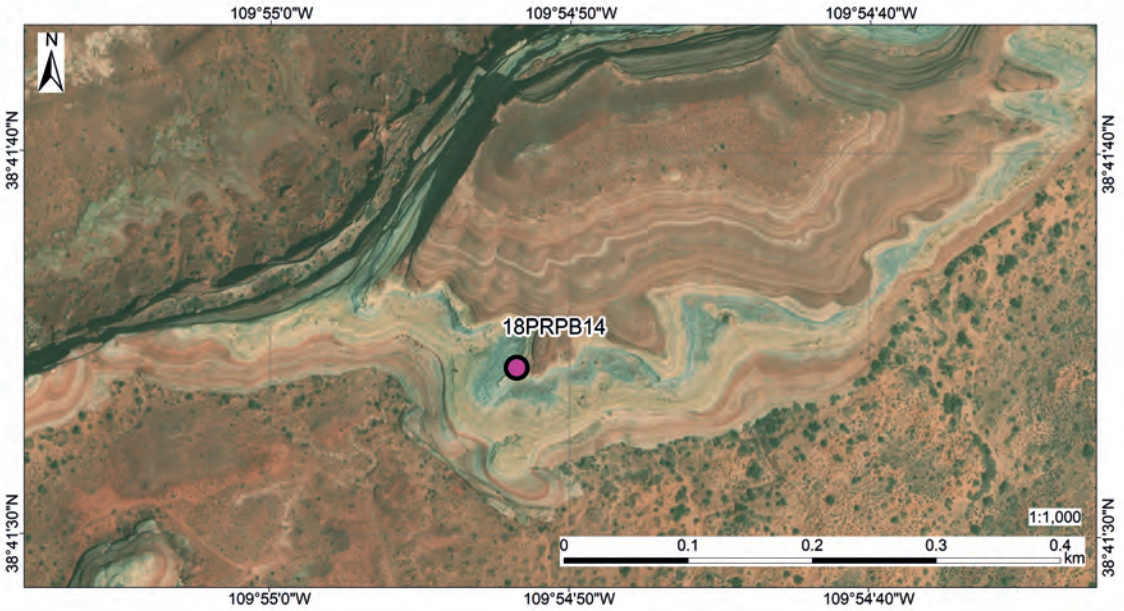

Figure DR1: Sample 18PRPB14 location (Rainbow Rocks Sandstone). Satellite image of the outcrop (top), photographs of sample locality (middle), geological map showing locations of 18PRPB14 and MF006 (Courthouse Fault) (bottom). Geological map from Doelling (2002).

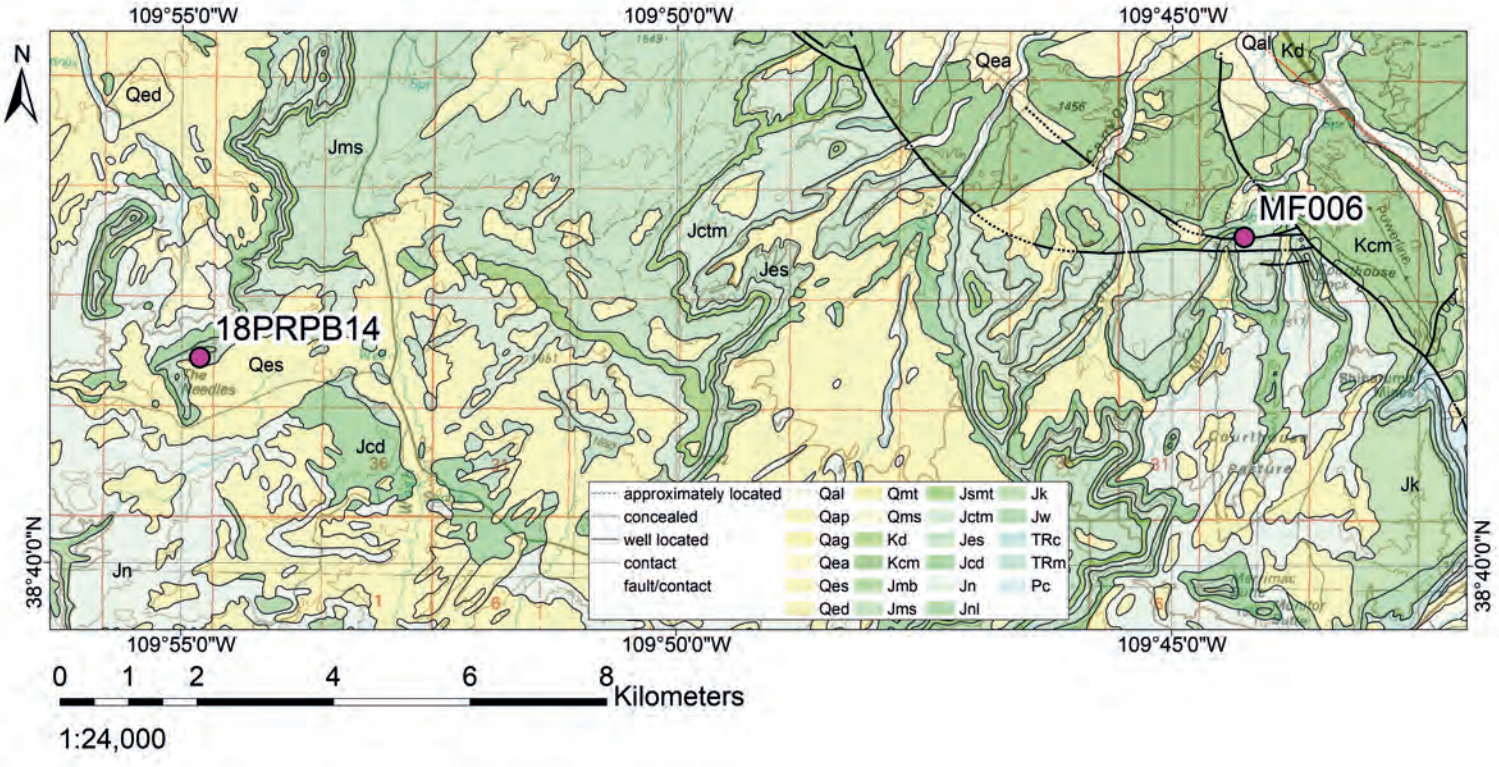

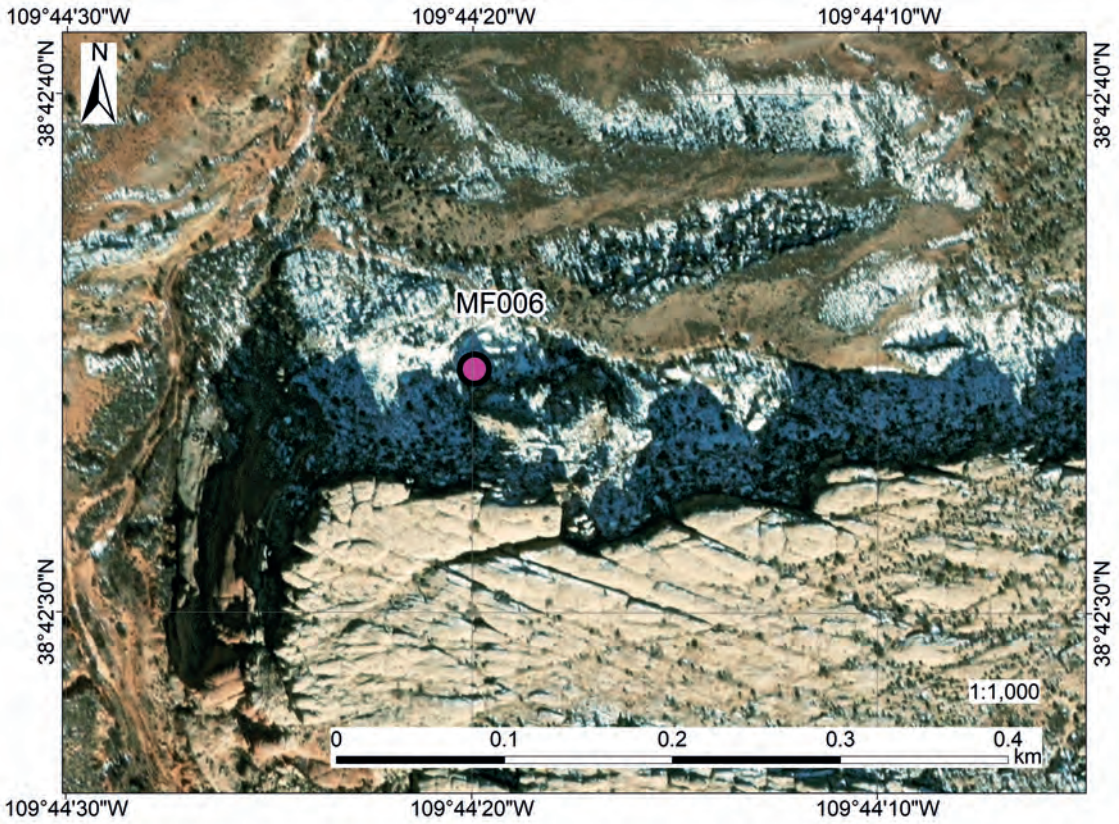

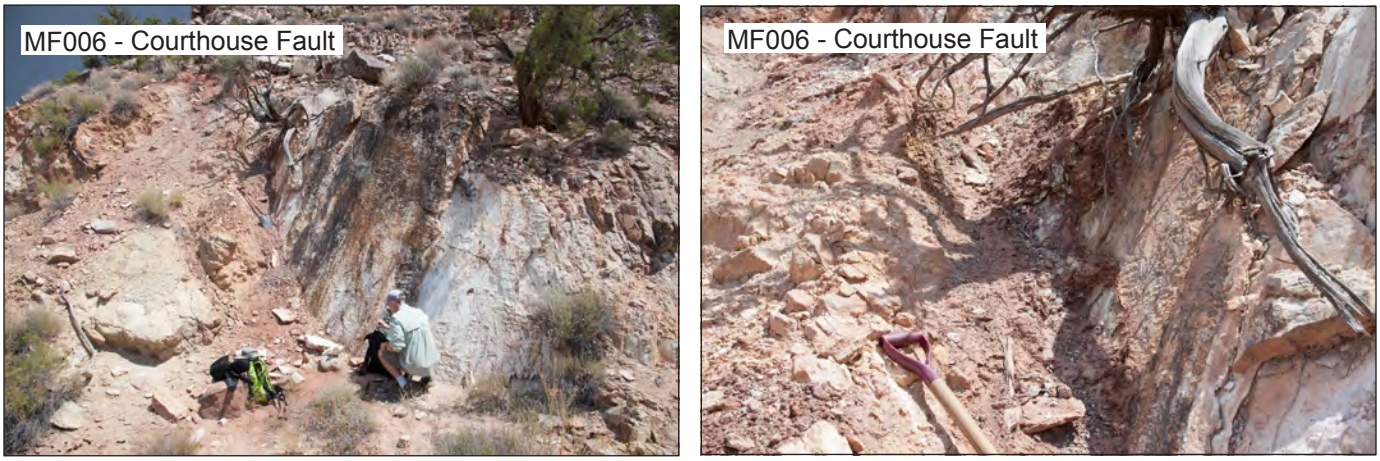

Figure DR2: Sample MF006 location (Courthouse Fault). Satellite image of the outcrop (top), and photographs of sample locality (bottom).

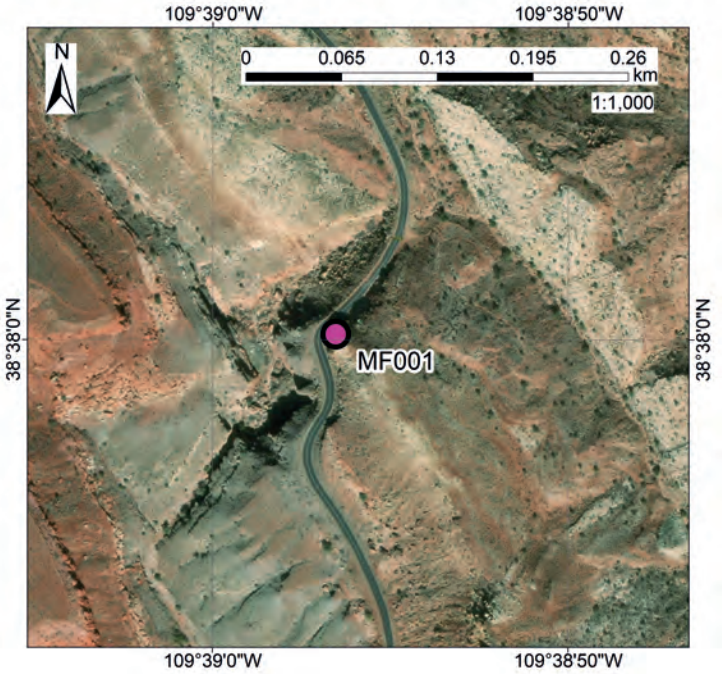

Figure DR3: Sample MF001 location (Moab Fault). Satellite image of the outcrop (top), photographs of sample locality (middle), geological map showing location of MF001 (bottom). Geological map from Doelling (2002).

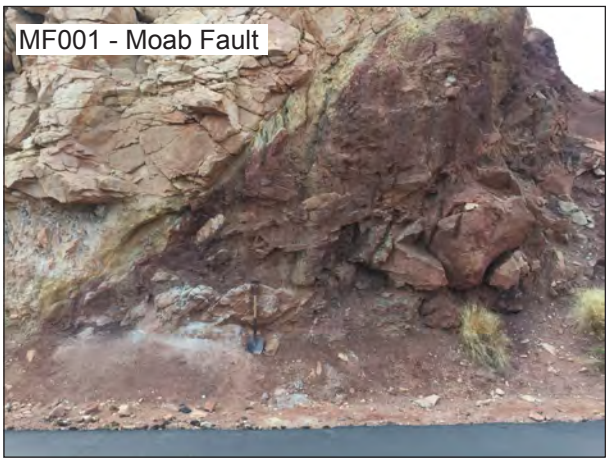

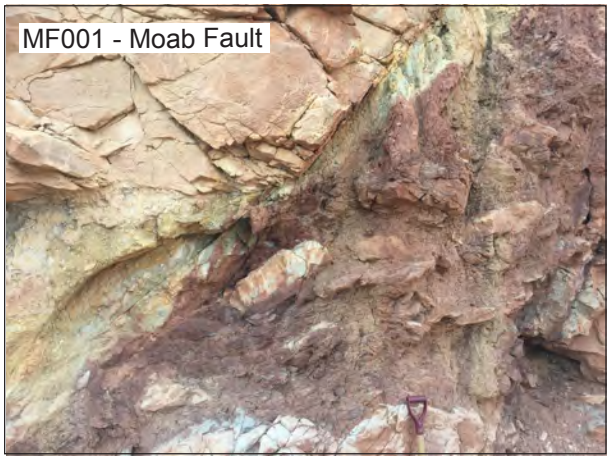

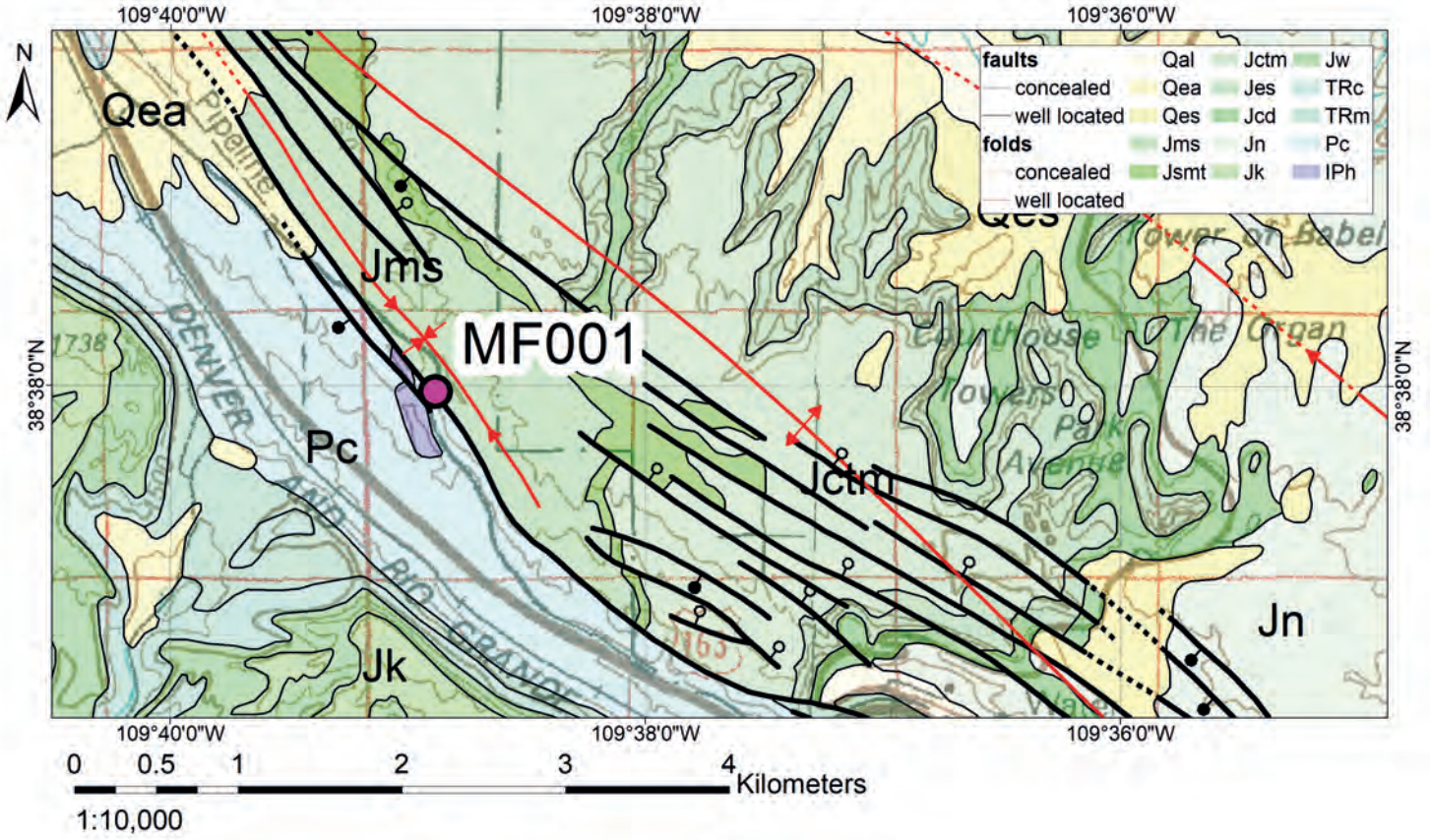

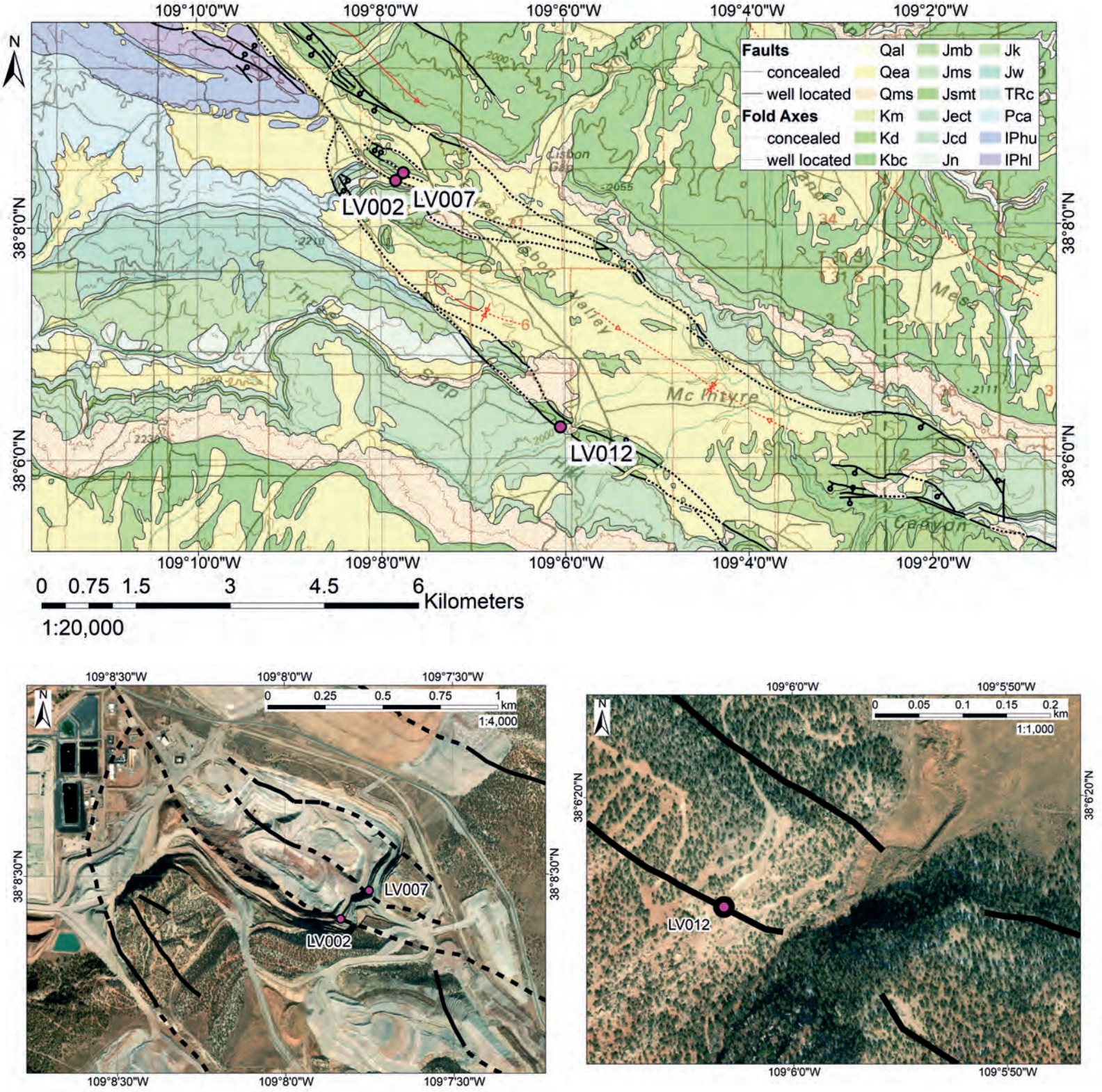

Figure DR4: Geological map showing locations of Lisbon Valley fault gouge samples (top) - LV002 (Lisbon Valley Fault), LV007 (Keystone Fault), and LV012 (GTO Fault). Satellite images of sample locations (bottom). Geological map from Doelling (2004).

Figure DR5: Outcrop photographs of samples LV002 (Lisbon Valley Fault), LV007 (Keystone Fault), and LV012 (GTO Fault)

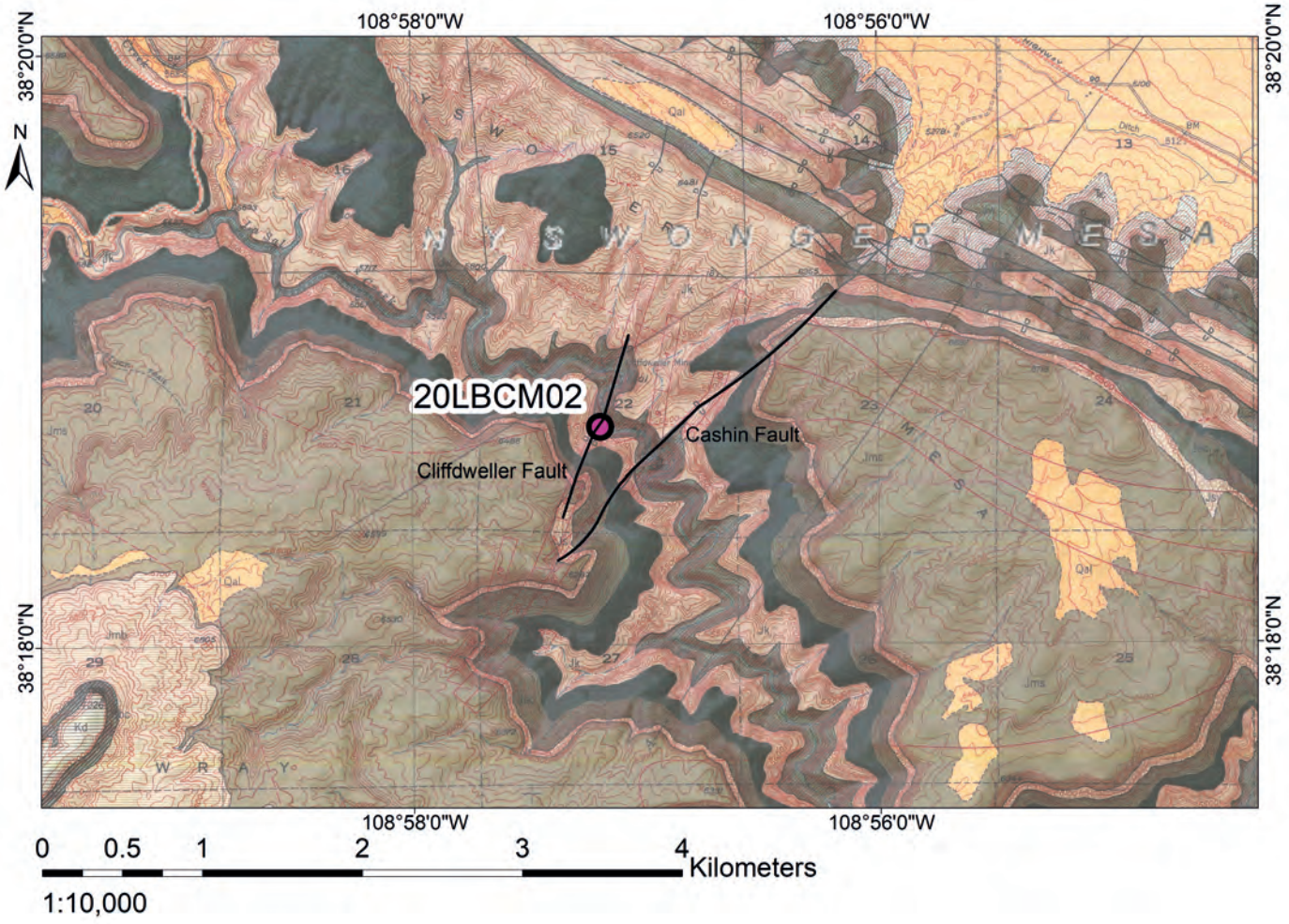

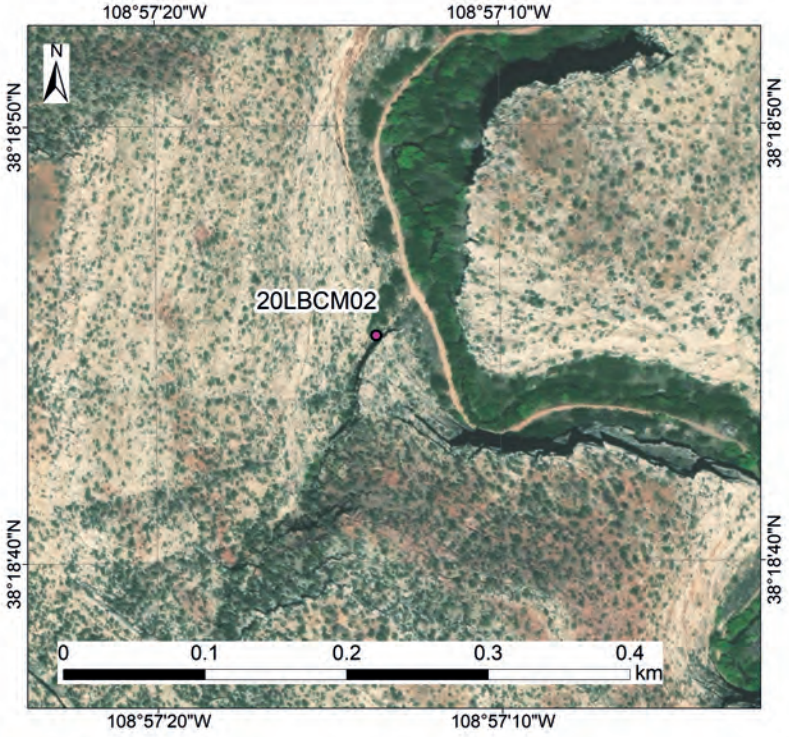

Figure DR6: Sample 20LBCM02 location (Cliffdweller Fault). Geological map showing location (top), satellite image of the outcrop (bottom left), photographs of sample locality (bottom right). Geological map from Withington (1955).

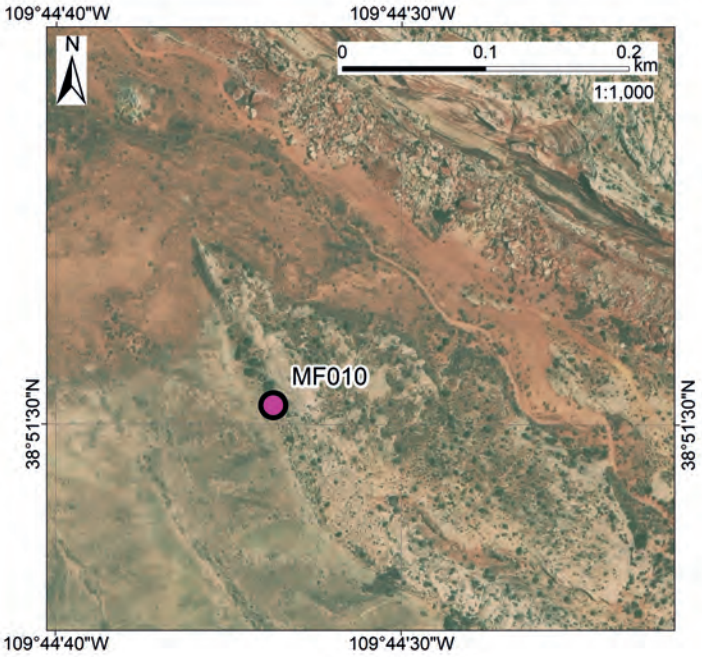

Figure DR7: Sample MF010 location (Salt Valley Fault). Satellite image of the outcrop (top), photographs of sample locality (middle), and geological map showing location (bottom). Geological map from Doelling (2002).

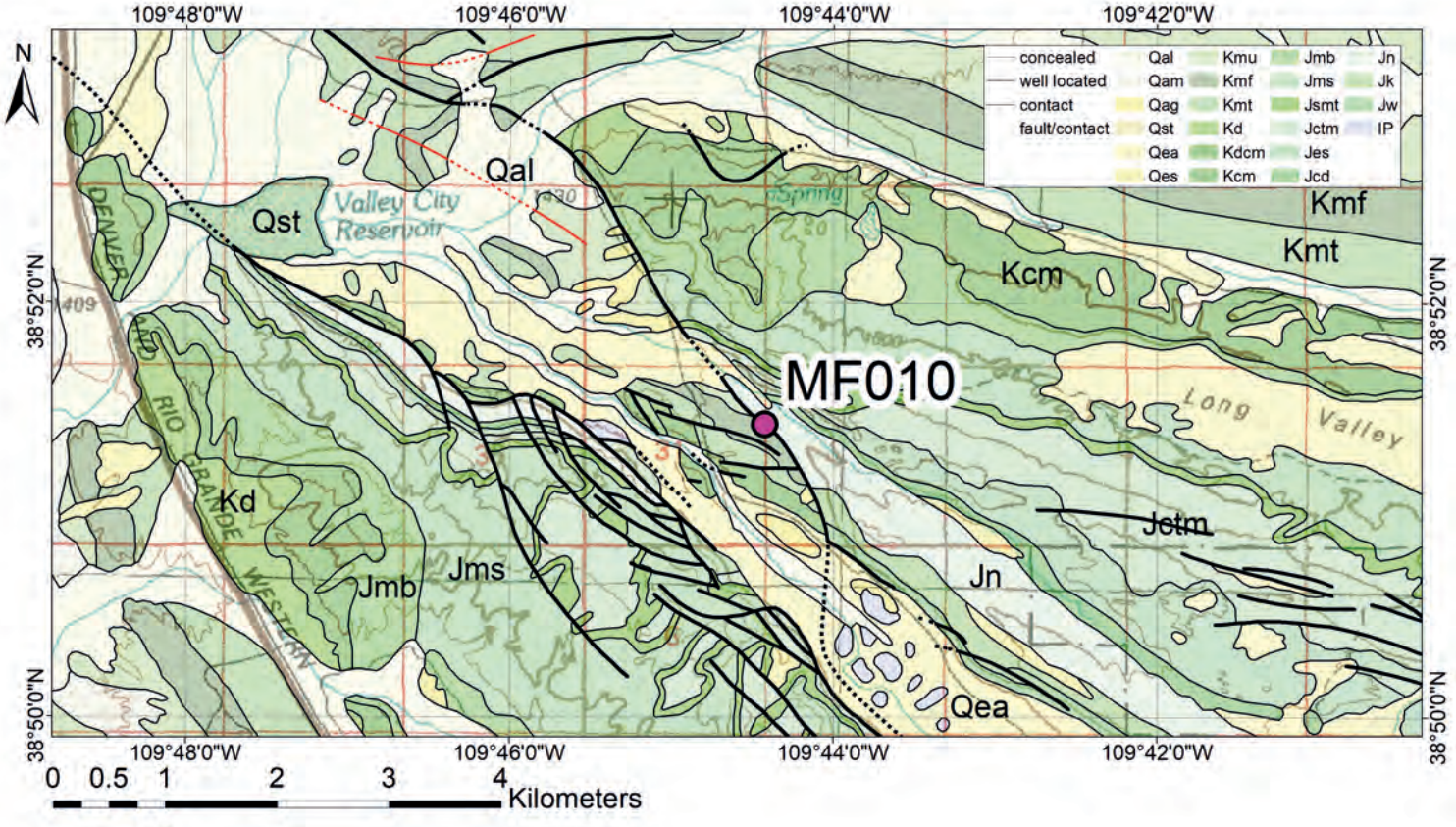

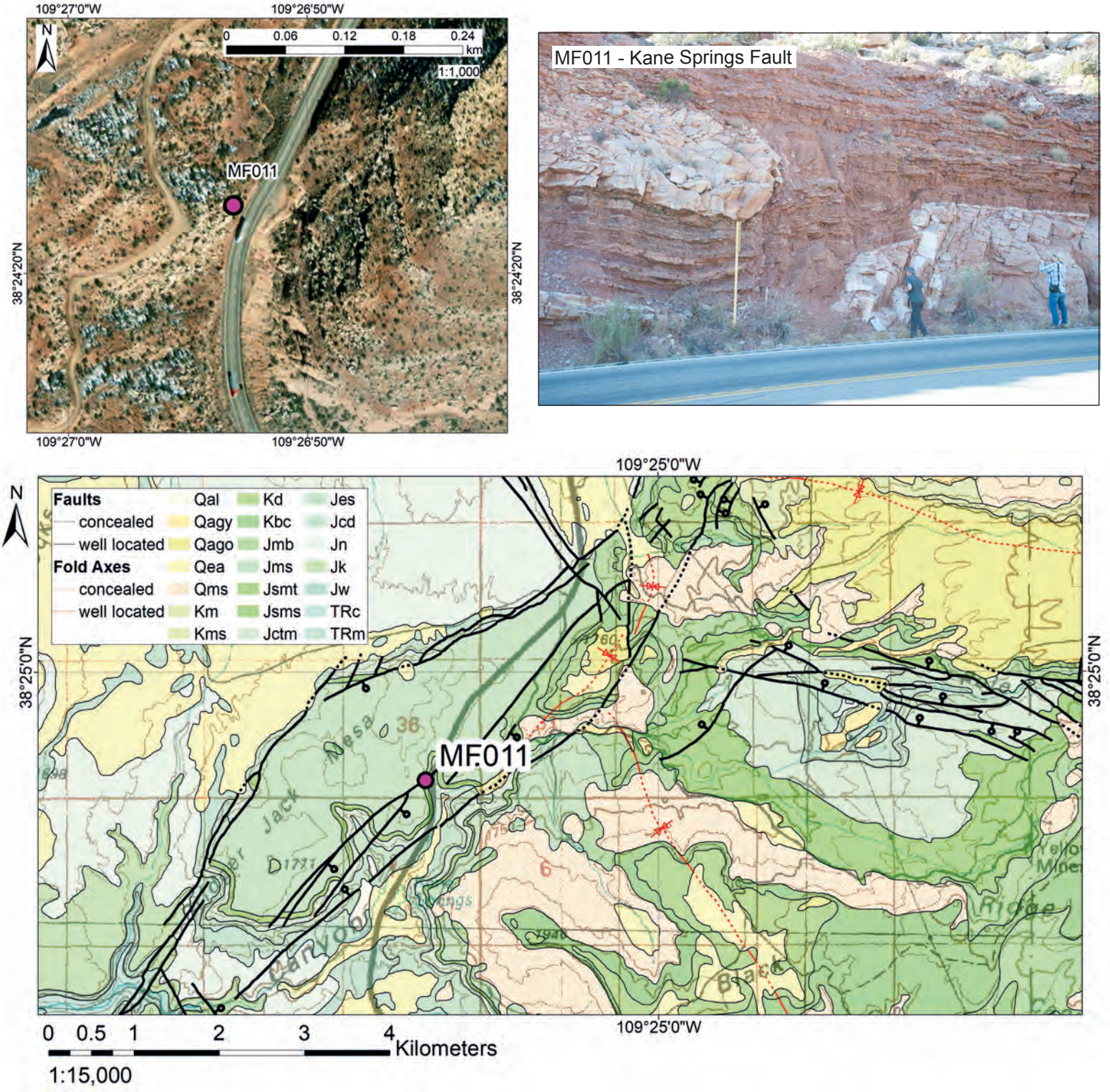

Figure DR8: Sample MF011 location (Kane Springs Fault. Satellite image of the outcrop (top left), photographs of sample locality (top right), and geological map showing location (bottom). Geological map from Doelling (2004).

METHODS

CLAY SAMPLE SEPARATION PROCEDURES

Sample Processing

Samples of fault gouge and sandstone were gently disaggregated by hand, suspended in DI water, and ultrasonically agitated. We took extra care to minimize mechanical size reduction and avoid over-crushing of coarse K-rich minerals. We then gravity settled the samples in a large 2 liter Teflon container to separate the <2 μm clay fraction, which we centrifuged at various speeds and durations to extract four size fractions: 1-2 μm, 0.2-1 μm, 0.05-0.2 μm, and <0.05 μm. Samples were air-dried under a heat lamp and did not exceed 60 °C.

Illite Polytypes and Powder X-ray Diffraction

Illite occurs as several different polytypes that reflect the arrangement of clay mineral interlayering and stacking sequence of the silicate sheets. Typically, illite in fault gouge and sedimentary basins consist of a mixture of the $2M_1$ and $1M_d$ polytypes. The $2M_1$ polytype is most stable and generally forms above 280 °C (e.g., Yoder & Eugster 1955, Srodon & Eberl 1984), interpreted to represent detrital material. The $1M_d$ polytype is the disordered endmember and usually forms at temperatures below 200 °C during diagenesis or from fluid-rock interactions. The amount of $2M_1$ and $1M_d$ illite polytypes can be quantified from XRD patterns of randomly oriented samples.

We gently chopped each size fraction with a razor blade and passed them through a 110-micrometer mesh. We loaded the powder for each size fraction into a side-loading sample holder to achieve a high degree of particle randomness. We analyzed all size fractions of each sample on a Bruker D8 Powder Diffractometer that uses CuKα radiation with a scintillation detector at the University of Arizona. We scanned each sample from 16 to 44° 2Θ with a step size of 0.05° at 40 seconds per step. Polytype quantification was done by Rietveld Refinement of the powder X-ray diffraction data using BGMN® and the Profex graphical user interface (Doebelin and Kleeberg, 2015; Boles et al., 2018). Reitveld Refinement has been shown to accurately model the proportions of illite polytypes in random mixtures (Boles et al., 2018).

K-Ar Dating

Following XRD, each of the size fractions were dated using the K-Ar method. Ar isotope compositions were analyzed at the Argon Geochronology for the Earth Sciences Lab at Lamont-Doherty

Earth Observatory. Sample aliquots were weighed with a microbalance and loaded into planchets and evacuated to ultra-high vacuum in an extraction line with a zinc-selenide window. Standardization was achieved by measurements of air pipettes and aliquots of GLO-1 glauconite reference material. Each sample was measured in duplicate to estimate the variability and if the difference between the two measurements was greater than 10%, further measurements were made. Samples were degassed in one step in vacuo with a CO_2 laser, and the gas was exposed to hot zirconium-aluminum getters to remove active species prior to admitting in to a VG 5400 noble gas mass spectrometer where the Ar was measured in static peak-hopping mode on an analogue multipler following the procedure of Hemming et al., (2002) K concentration measurements were made by ICP-MS at the Arizona Laboratory for Emerging Contaminants. Sample aliquots were dissolved in Parr pressure digestion vessels, diluted, and analyzed for K, other major cations, and trace metal concentrations.

We correlated the apparent K-Ar ages and percent $2M_1$ illite of all size fractions by implementing York-type weighted linear regression using the maximum likelihood method (Thirumalai et al., 2011). The extrapolated end-member values represent unmixed authigenic and detrital components, and authigenic age is the mean integrated age of the time interval over which illite grew (Pevear, 1999; Ylagan et al., 2002). The percentage of detrital illite is linearly related to the decay constant of potassium, so therefore is plotted against $e^{\lambda t}$-1 instead of date/age.

Errors on the ages include uncertainties from Ar measurements, K measurements, and XRD illite polytype determinations. The uncertainties on illite polytypes were calculated from the estimated standard deviations of each Rietveld refinement analysis.

Rb-Sr Dating

Approximately 15-25 mg of the <0.05um fraction from the above clay separation procedures was leached with 1 M HCl for 15 minutes (Clauer et al., 1993) in a polypropylene centrifuge tube. After centrifugation at 6000 rpm for 15 minutes, the supernatant was discarded, and the residue rinsed multiple times with Milli-Q water (Millipore, 18.2 MΩ cm). The residue was then weighed precisely in a 9ml Teflon jar along with appropriate amounts of ^{87}Rb and ^{84}Sr spike solutions (Oak Ridge National Laboratory, 99.64% ^{84}Sr and 99.16% ^{87}Rb). The residue was dissolved with 1ml 29N HF and 0.25 ml 16N HNO_3 and heated at 125 degrees C for 24 hours. The completely dissolved samples-spike solution was dried and taken up in 2.5 HCl for separation of Rb from Sr by cation column chemistry using Dowex AG 50 WX8 (50–100mesh) cation exchange resin. The Sr containing cut was dried and dissolved in 8N HNO_3

and purified using Sr resin (Sr-Spec Resin®, Eichrom, Lisle, Illinois, Part number SR-B100-A) using procedures modified from Horwitz et al., 1992. Both Rb and Sr were loaded onto tantalum filaments using a TaF_5 activator (Charlier et al., 2006) to enhance ionization.

Rubidium and Strontium were analyzed using a VG Sector 54 multi-collector thermal ionization mass spectrometer in static and dynamic collection mode, respectively at the University of Arizona. The $^{87}Sr/^{86}Sr$ ratios are corrected for mass fractionation using an $^{86}Sr/^{88}S$ ratio of 0.1194. During the study, the $^{87}Sr/^{86}Sr$ of NIST SRM 987 standards analyzed with the samples yielded a value of 0.710264 ± 0.00001 (n = 5), and sample ratios were normalized to 0.710245 (Faure and Mensing, 2005). Fractionation of Rb was corrected with a natural $^{87}Rb/^{85}Rb$ ratio of 0.3857 (Berglund and Wieser, 2011). Based on long term analyses, the external reproducibility was estimated to be ± 1.5% for $^{87}Rb/^{86}Sr$ and ± 0.05% for $^{87}5r/^{86}Sr$. Total process blanks were an insignificant proportion of the total rubidium and strontium separated from each sample. Isoplot 4.15 (Ludwig, 2012) and a Rb decay constant of 1.3972×10^{-11} (Villa et al., 2015) were used for age regressions (Fig. 3).

Re-Os Dating

Approximately 0.1 g or 0.4g of handpicked bornite or chalcocite, appropriate weights of ^{185}Re- and ^{190}Os-enriched spikes, 12 ml of reverse aqua regia ($1HCl:3HNO_3$) and 2 ml of H_2O_2 were added to borosilicate glass Carius tubes. The sample, spikes, and reagents were sequentially frozen in an ethanol-liquid nitrogen slurry and sealed with a gas-oxygen torch. The sealed tubes were then heated to approximately 240°C for 24 hours in an oven. Following dissolution and sample-spike homogenization, the frozen Carius tubes were opened and transferred to Teflon distillation vessels. An additional 2ml of H_2O_2 was added and the Osmium was distilled for two hours at 100-110°C into cold HBr. After drying, the HBr and contained Os was purified using the microdistillation technique of Birck et al., (1997). Rhenium was separated and purified using anion exchange columns modified from (Morgan and Walker, 1989).

The purified Re was loaded onto Ni filaments with the addition of $Ba(NO_3)_2$ and Os fractions were loaded onto Pt filaments along with $Ba(OH)_2$. Samples were analyzed on a VG 54 mass spectrometer using an electron multiplier for Os and Faraday collectors for Re, with standard negative thermal ion mass spectrometer (NTIMS) techniques (Creaser et al., 1991). Total procedural Os blanks were approximately 0.1 pg and 10 pg for Re. Corrections from Re blanks were insignificant, while Os blank corrections were relevant and corrected using blank isotopic composition of $^{187}Os/^{188}Os = 0.181$. In-house Os and Re

standard solutions during the period of analysis give $^{187}Os/^{188}Os$ ratios of 0.149718 ± 0.00047 (1 S.D., n = 8) and 0.59613 ± 0.00079 (1 S.D., n = 8). Uncertainties for the isotopic ratios were propagated and include uncertainties in the spike calibration, mass spectrometric analysis and blank concentration variation (Table DR5).

Isoplot 4.15 (Ludwig, 2012), a Re decay constant of 1.666×10^{-11} (Smoliar et al., 1996) and error correlation factors (rho) were used for age regressions (Fig. 3 & Fig. DR10). Total common Os for the chalcocite samples were under 10pg and 80-100 pg for Bornite. Because of their low common Os ($^{187}Re/^{188}Os$ of 500,000+), a ^{187}Re-^{187}Os concentration isochron was used for chalcocite whereas the bornite common Os was sufficiently elevated to precisely measure ^{188}Os and therefore normal $^{187}Re/^{188}Os$-$^{187}Os/^{188}Os$ isochrons are reported.

DATA TABLES & ISOCHRON PLOTS

TABLE DR2: SAMPLE COMPOSITION FROM XRD IN %

Sample ID	Size fraction (μm)	1Md illite	2M1 illite	Kaolinite	Smectite	Quartz	K-feldspar	Plagioclase	Calcite	Hematite	Other
Rainbow Rocks	1.0 - 2.0	14.2	10.0	10.9	24.9	15.1	11.1	1.0	12.6	0.2	
Sandstone	0.2 - 1.0	22.4	3.1	60.8	12.1	-	1.0	0.4	0.3	-	
	0.05 - 0.2	51.1	5.1	15.0	26.5	-	1.6	0.5	-	0.1	
	<0.05	53.3	3.8	9.2	26.0	1.0	3.5	-	2.5	0.7	
Keystone Fault	1.0 - 2.0	12.9	5.3	40.5	3.7	32.4	2.3	0.9	1.4	0.6	
	0.2 - 1.0	69.0	2.0	15.9	6.5	5.8	-	0.3	0.1	0.2	
	<0.2	40.0	8.0	10.0	29.0	1.9	0.2	7.7	0.2	-	3.4 (chlorite)
Lisbon Valley Fault	1.0 - 2.0	37.0	6.6	34.0	12.0	8.3	0.4	-	-	2.9	
	0.2 - 1.0	53.0	5.3	12.0	14.0	3.8	2.1	6.0	-	3.3	
	0.05 - 0.2	75.0	2.0	13.0	3.7	-	0.1	5.6	-	0.4	
	<0.05	65.0	0.4	13.4	6.0	0.4	0.9	9.2	3.8	0.3	
GTO Fault	1.0 - 2.0	23.0	3.3	13.3	28.0	9.2	-	0.1	7.7	0.3	
	0.2 - 1.0	28.0	3.1	38.0	18.0	4.8	1.1	1.2	4.8	0.4	
	<0.2	37.0	1.1	34.0	21.0	-	0.5	0.3	2.3	-	3.4 (chlorite)
Kane Springs Fault	1.0 - 2.0	29.0	4.6	26.0	20.0	8.1	2.5		5.2	3.7	
	0.2 - 1.0	40.0	4.1	22.0	28.0	1.8	1.7	0.5	-	2.0	
	0.05 - 0.2	25.8	2.5	64.0	6.0	-	0.5	0.3	-	0.2	
	<0.05	58.0	0.5	20.0	-	0.1	0.9	-	7.7	0.1	12.4 (aragonite)
Moab Fault	1.0 - 2.0	17.2	5.2	64.0	7.0	0.9	3.0	-	0.5	2.3	
	0.2 - 1.0	38.3	7.6	20.6	18.9	1.3	-	1.5	-	8.8	3.0 (chlorite)
	0.05 - 0.2	36.0	0.5	44.0	17.0	0.1	0.8	-	0.1	1.2	
	<0.05	30.2	1.9	39.0	18.5	0.2	0.8	9.1	-	0.5	
Courthouse Fault	1.0 - 2.0	41.2	4.8	30.6	14.8	6.8	-	0.4	0.1	1.3	
	0.2 - 1.0	53.8	5.8	10.4	23.4	2.7	2.0	-	-	1.8	
	<0.2	24.8	0.8	57.5	13.9	-	-	-	-	0.4	2.6 (chlorite)
Salt Valley Fault	1.0 - 2.0	6.7	6.3	57.5	20.9	5.7	1.7	-	-	0.2	1.0 (gypsum)
	0.2 - 1.0	9.5	2.4	74.6	12.0	0.3	0.9	0.2	-	-	
	0.05 - 0.2	28.7	2.5	44.1	21.4	-	0.9	2.2	-	0.2	0.1 (gypsum)
Cliffdweller Fault	1.0 - 2.0	53.5	3.1	-	4.8	12.6	8.1	-	-	-	17.8 (sanidine)
	0.2 - 1.0	56.8	2.3	14.6	15.0	0.7	5.3	-	-	-	3.8 (chlorite), 2.1 (gibbsite)
	<0.2	62.4	0.7	27.0	7.4	-	-	-	-	-	2.0 (chlorite)

TABLE DR3: PROPORTION ILLITE, POTASSIUM %, & GAS AGES											
Sample ID	Size fraction (μm)	1Md illite (%)	2M1 illite (%)	K (%)	Total gas age (Ma)	Uncertainty (1s)	e(λt)-1	100% 1Md age (Ma)	Uncertainty (1s)	100% 2m1 age (Ma)	Uncertainty (1s)
Rainbow Rocks	1.0 - 2.0	58.68	41.32	3.89	142.1	3.70	0.0820	41.1	2.5	267.0	5.2
Sandstone	0.2 - 1.0	87.84	12.16	4.53	74.7	0.40	0.0423				
	0.05 - 0.2	90.93	9.07	4.75	66.0	1.10	0.0373				
	<0.05	93.35	6.65	5.01	57.0	0.40	0.0321				
Keystone Fault	1.0 - 2.0	70.88	29.12	2.04	97.7	1.30	0.0556	65.2	1.0	174.0	11.2
	0.2 - 1.0	97.18	2.82	4.48	68.5	0.60	0.0387				
	<0.2	83.33	16.67	4.73	81.5	4.90	0.0462				
Lisbon Valley Fault	1.0 - 2.0	84.86	15.14	4.71	78.0	0.98	0.0442	45.3	0.9	254.1	18.6
	0.2 - 1.0	90.91	9.09	5.14	67.7	1.03	0.0382				
	0.05 - 0.2	97.4	2.6	5.96	50.3	0.60	0.0283				
	<0.05	99.4	0.6	5.27	47.4	0.55	0.0266				
GTO Fault	1.0 - 2.0	87.45	12.55	2.65	97.3	4.45	0.0554	48.1	2.6	156.6	20.7
	0.2 - 1.0	90.03	9.97	3.86	61.2	6.94	0.0345				
	<0.2	97.11	2.89	4.43	49.1	8.16	0.0276				
Kane Springs Fault	1.0 - 2.0	86.31	13.69	4.48	106.5	7.55	0.0608	47.7	3.8	401.4	49.1
	0.2 - 1.0	90.7	9.3	4.91	83.3	0.34	0.0473				
	0.05 - 0.2	91.17	8.83	4.55	82.1	0.78	0.0466				
	<0.05	99.15	0.85	4.72	51.4	3.21	0.0289				
Moab Fault	1.0 - 2.0	76.92	23.08	5.75	281.5	6.57	0.1689	59.1	5.7	879.9	101.8
	0.2 - 1.0	83.44	16.56	4.45	252.8	1.80	0.1504				
	0.05 - 0.2	98.63	1.37	5.26	102.5	0.10	0.0585				
	<0.05	94.08	5.92	4.71	115.2	0.51	0.0659				
Courthouse Fault	1.0 - 2.0	89.57	10.43	4.31	61.6	2.78	0.0347	41.9	2.3	228.8	40.1
	0.2 - 1.0	90.27	9.73	4.01	61.5	1.53	0.0347				
	<0.2	96.88	3.13	5.26	48.1	0.70	0.0270				
Salt Valley Fault	1.0 - 2.0	51.53	48.47	1.84	130.7	1.1	0.0751	47.5	3.1	209.3	15.1
	0.2 - 1.0	79.97	20.03	2.17	81.4	1.2	0.0462				
	0.05 - 0.2	91.99	8.01	3.46	61.3	1.0	0.0346				
Cliffdweller Fault	1.0 - 2.0	94.5	5.5	6.82	128.2	3.5	0.0736	43.3	4.6	1221.0	195.0
	0.2 - 1.0	96.08	3.92	4.44	115.6	7.3	0.0662				
	<0.2	98.89	1.11	5.21	60.7	1.8	0.0342				

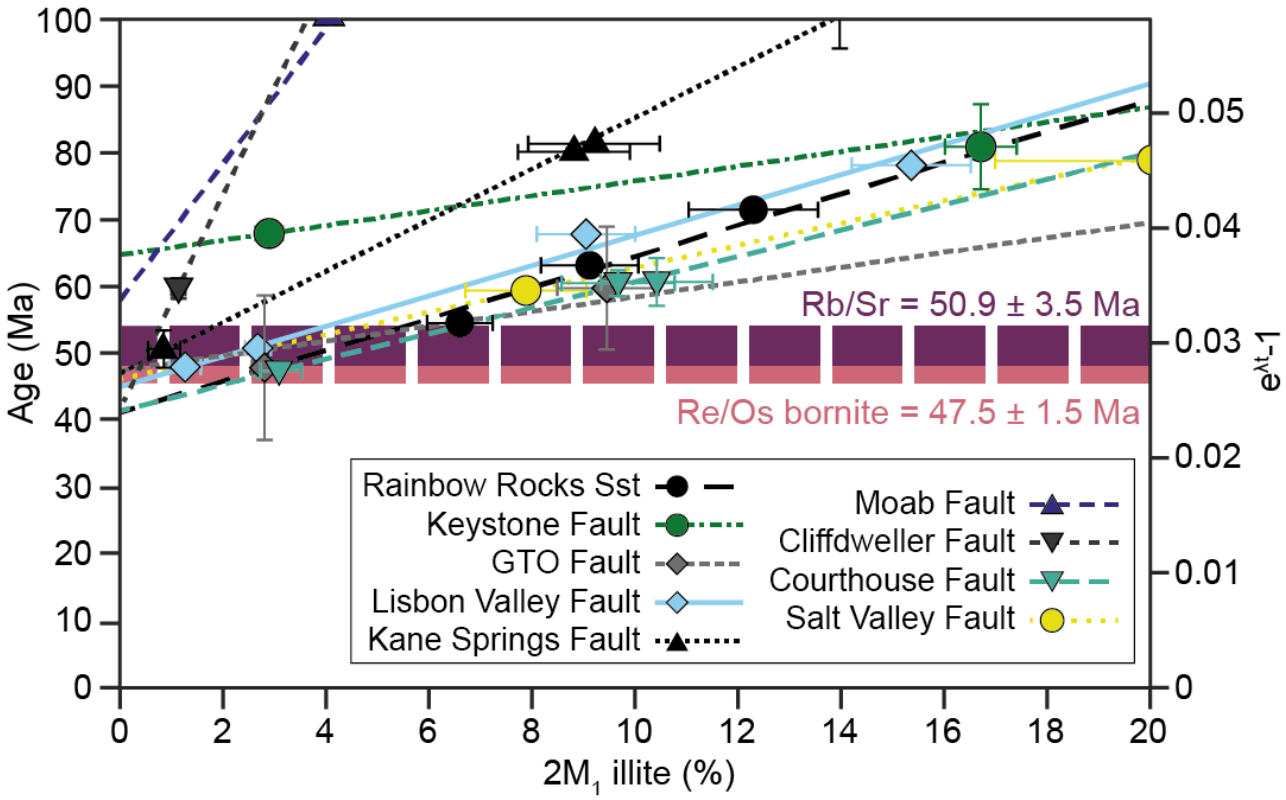

Figure DR9: Illite Age Analysis plots of analyzed samples, zoomed in to the lower left quadrant (See Fig. 2 in main text). $\lambda = 5.543*10^{-10}$ (Min et al., 2000).

TABLE DR4: Rb/Sr DATA					
Sample ID	Material	$^{87}Rb/^{86}Sr$	± (%)	$^{87}Sr/^{86}Sr$	± (%)
Lisbon Valley					
LVF-1	Residue	14.12	2	0.72189	0.05
LVF-2	Residue	8.98	2	0.71779	0.05
LVF-3	Residue	11	2	0.71921	0.05
LVF-4	Residue	10.69	2	0.71911	0.05
Keystone Fault					
KSF-1	Residue	1.23	2	0.71215	0.05
KSF-2	Residue	1.31	2	0.71229	0.05
KSF-3	Residue	1.3	2	0.71242	0.05
GTO Fault					
GTOF-1	Residue	2.53	2	0.71332	0.05
GTOF-2	Residue	2.65	2	0.71348	0.05
GTOF-3	Residue	2.77	2	0.71357	0.05
GTOF-4	Residue	2.66	2	0.71345	0.05

TABLE DR5: BORNITE Re/Os DATA												
Sample ID	Material	Re (ppb)	± (absolute)	Os (ppb)	± (absolute)	^{187}Os (ppb)	± (absolute)	$^{187}Re/^{188}Os$	± (absolute)	$^{187}Os/^{188}Os$	± (absolute)	rho
Bed15-B1	Bornite	1842.7	1.7	1.14	0.01	1.06	0.01	105814	1092	96.66	1.38	0.719
Bed15-B2	Bornite	1873.8	1.8	1.12	0.01	1.05	0.01	126761	1360	112.97	1.67	0.721
Bed15-B3	Bornite	1568.2	1.5	1.03	0.01	0.94	0.01	78092	782	74.25	1.06	0.694
Bed15-B4	Bornite	1793.6	1.5	1.10	0.01	1.02	0.01	109392	1219	99.25	1.61	0.683
Bed15-B5	Bornite	1834.0	2.1	1.19	0.01	1.09	0.01	87609	843	82.79	1.18	0.667

TABLE DR6: CHALCOCITE Re/Os DATA								
Sample ID	Material	Re (ppm)	± (absolute)	^{187}Re (ppb)	± (absolute)	^{187}Os (ppb)	± (absolute)	Moly model age (Ma)
LV-17-1-A	Chalcocite	657.844673	2.965073	411.821949	1.856186	0.838703	0.003222	121.601124
LV-17-1-B	Chalcocite	770.810702	3.472988	482.540603	2.174149	0.972963	0.003732	120.394225
LV-17-1-C	Chalcocite	819.976726	3.715055	513.319370	2.325687	1.038852	0.003982	120.839104
LV-17-1-D	Chalcocite	694.333839	3.129490	434.664787	1.959114	0.881123	0.003386	121.038322

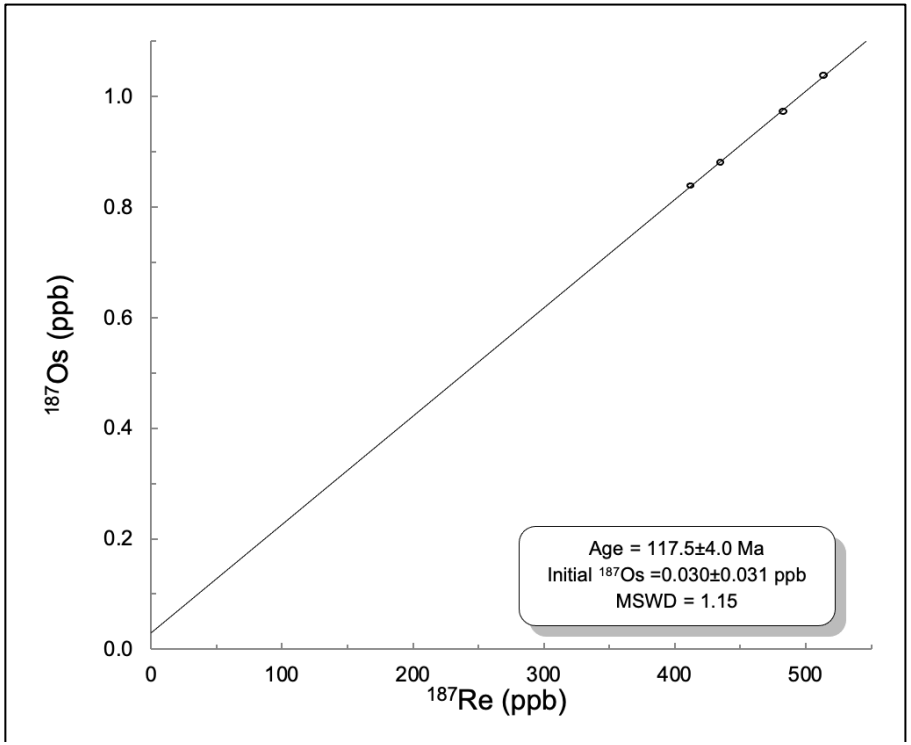

Figure DR10: Re-Os concentration isochron for Lisbon Valley chalcocite.

DISCUSSION ON DRIVERS OF FAULTING AND FLUID FLOW

Faulting and fluid flow driven by stress-changes

Surrounding the Paradox Basin are several basement-cored uplifts that formed by reactivation of basement shear zones during the Laramide Orogeny which started 80-75 Ma (Coney, 1971; Dumitru et al., 1994; Bird, 1998; Bump and Davis, 2003; Davis and Bump, 2009; Tindall et al., 2010), and compressive deformation possibly ceased by 35-40 Ma (Coney, 1971; Dickinson et al., 1988; Bird, 1998). It is possible that our younger phase of fault activity is related to late-stage Laramide deformation. Alternatively, post-Laramide 'relaxation' driven by the release of stored elastic strain following Laramide shortening may be responsible, or a renewed phase of salt movement and/or dissolution caused widespread fault reactivation across the Paradox Basin (Solum et al., 2010).

Faulting and fluid flow driven by exhumation

Rapid erosional exhumation and incision can lead to the formation of high relief topography along with high hydraulic gradients, where we can expect deeper circulation of meteoric waters recharged at higher elevations (McIntosh and Ferguson, 2021). This process can sweep reduced, hydrocarbon-bearing fluids into shallower formations along discharge zones such as faults, a process possibly responsible for the flow of hydrocarbons in the Rainbow Rocks paleo-oil reservoir (cite). Rocks younger than ~75 Myr are mostly missing from the Paradox Basin due to Pliocene erosional exhumation of the Colorado Plateau (e.g., Murray et al., 2016), which leads to large uncertainties in burial-history models, and further complications arise from salt tectonism (Nuccio and Condon, 1996; Rasmussen and Rasmussen, 2009), resulting in a poorly constrained exhumation history of the Paradox Basin ~75-6 Ma. Several low temperature thermochronology studies focused on the Colorado Plateau interior suggest a Middle Cenozoic Cooling Event 30-20 Ma (Murray et al., 2019), and rapid erosional exhumation within the last 6 Myr (e.g., Murray et al., 2016; 2019). It is unclear if the Paradox Basin experienced significant exhumation and increased topographically driven flow during the Eocene.

Faulting and fluid flow associated with slab roll-back, magmatism, and hydrothermal fluids

The timing of faulting and associated mineralization from this study fits into a broader regional pattern of magmatic activity and mineralization. Carlin-type mineralization associated with hydrothermal fluids occurred in the Eocene (~37-38.5 Ma) in northeastern Nevada (Hollingsworth et al., 2017). Magmatism and associated Pb-Zn-Ag deposits occurred in the Colorado Mineral Belt 38.5-44 Ma (Rosera et al.,

2021). Contour maps of radiometric ages of subduction-related magmatic rocks and mineralization show a younging trend towards the southeast, from 50 Ma in Idaho to 13 Ma in southern Nevada (Fig. DR4; Lipman et al., 1972; Coney and Reynolds, 1977; Best et al., 2013). It is hypothesized that this trend was caused by rapid steepening and rollback of the subducting Farallon slab (Coney and Reynolds, 1977), which triggered widespread extension and magmatism by exposing hydrated North American lithosphere to hot asthenosphere (Humphreys et al., 2003; Humphreys, 2009; Cassel et al., 2018). Magmatism increases heat flow and can drive fluid circulation in the crust, which plays a key role in mineralization. However, the trend becomes unclear across the Colorado Plateau, which appears to be little affected by intense magmatism experienced elsewhere in the Cordillera. The exceptions are the localized Henry, La Sal, and Abajo laccoliths that intruded 28 Ma (Nelson et al., 1992; Murray et al., 2016, 2019). Conversely, if contours are extended from the Colorado Mineral Belt and northern Nevada across the Paradox Basin, our 41-48 Ma ages fit broadly with the regional pattern. Therefore, it is possible that there was increased heat flow and circulation of fluids at this time due to Farallon slab-roll back and addition of mantle-derived heat to the base of the Colorado Plateau during the Eocene.

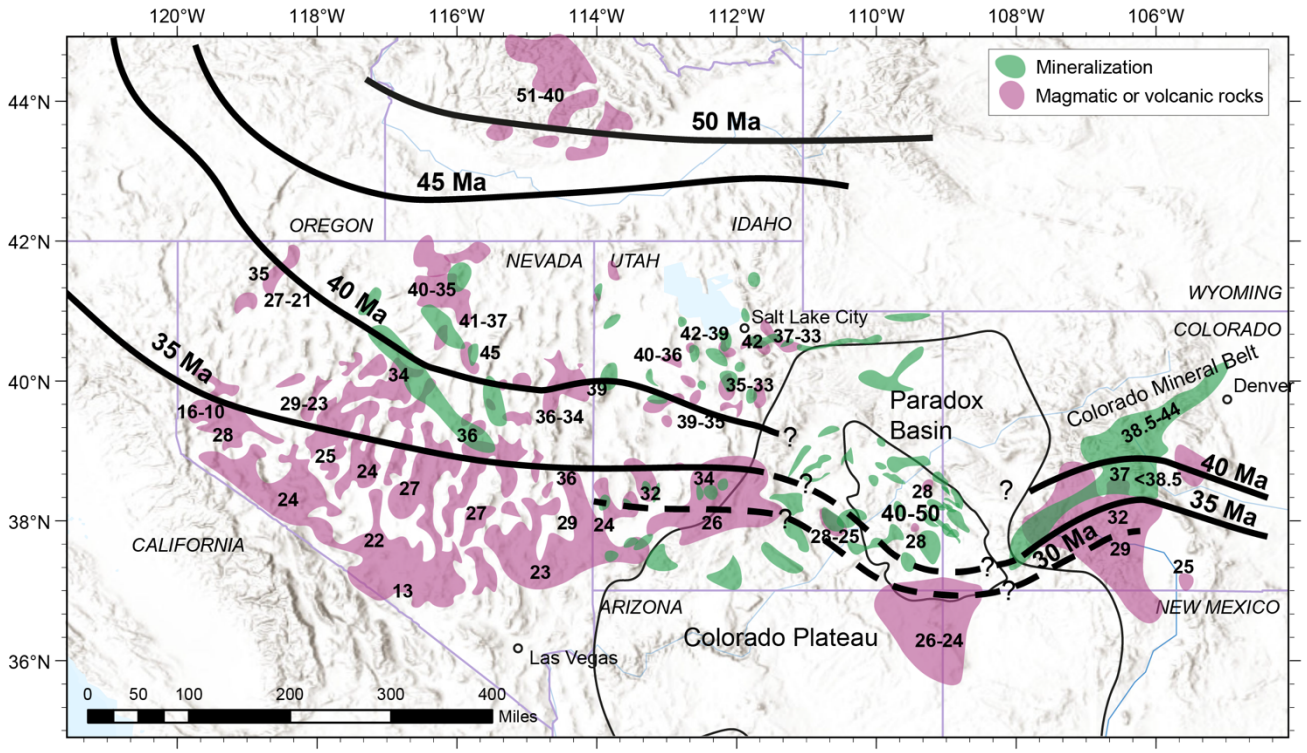

Figure DR11: Map of southwestern USA showing contours of radiometric ages of subduction-related magmatic rocks and mineralization.

REFERENCES

Berglund, M., and Wieser, M.E., 2011, Isotopic compositions of the elements 2009 (IUPAC Technical Report): Pure and applied chemistry, v. 83, p. 397–410.

Best, M.G., Christiansen, E.H., and Gromme, S., 2013, The 36-18 Ma southern Great Basin, USA, ignimbrite province and flareup: Swarms of subduction-related supervolcanoes: Geosphere, v. 9, p. 260–274, doi:10.1130/GES00870.1.

Birck, J.L., Barman, M.R., and Capmas, F., 1997, Re-Os Isotopic Measurements at the Femtomole Level in Natural Samples: Geostandards Newsletter, v. 21, p. 19–27, doi:10.1111/j.1751-908X.1997.tb00528.x.

Bird, P., 1998, Kinematic history of the Laramide orogeny in latitudes 35°-49°N, western United States: Tectonics, v. 17, p. 780–801, doi:10.1029/98TC02698.

Boles, A., Schleicher, A.M., Solum, J., and van der Pluijm, B., 2018, Quantitative X-Ray Powder Diffraction and the Illite Polytype Analysis Method for Direct Fault Rock Dating: A Comparison of Analytical Techniques: Clays and Clay Minerals, v. 66, p. 220–232, doi:10.1346/CCMN.2018.064093.

Bump, A.P., and Davis, G.H., 2003, Late Cretaceous–early Tertiary Laramide deformation of the northern Colorado Plateau, Utah and Colorado: Journal of Structural Geology, v. 25, p. 421–440, doi:10.1016/S0191-8141(02)00033-0.

Cassel, E.J., Smith, M.E., and Jicha, B.R., 2018, The Impact of Slab Rollback on Earth's Surface: Uplift and Extension in the Hinterland of the North American Cordillera: Geophysical Research Letters, v. 45, doi:10.1029/2018GL079887.

Charlier, B.L.A., Ginibre, C., Morgan, D., Nowell, G.M., Pearson, D.G., Davidson, J.P., and Ottley, C.J., 2006, Methods for the microsampling and high-precision analysis of strontium and rubidium isotopes at single crystal scale for petrological and geochronological applications: Chemical Geology, v. 232, p. 114–133, doi:10.1016/j.chemgeo.2006.02.015.

Clauer, N., Chaudhuri, S., Kralik, M., and Bonnot-Courtois, C., 1993, Effects of experimental leaching on Rb-Sr and K-Ar isotopic systems and REE contents of diagenetic illite: Chemical Geology, v. 103, p. 1–16, doi:10.1016/0009-2541(93)90287-S.

Coney, P.J., 1971, Cordilleran Tectonic Transitions and Motion of the North American Plate: Nature, v. 233, p. 462–465, doi:10.1038/233462a0.

Coney, P.J., and Reynolds, S.J., 1977, Cordilleran Benioff zones: Nature, v. 270, p. 403–406, doi:10.1038/270403a0.

Creaser, R.A., Papanastassiou, D.A., and Wasserburg, G.J., 1991, Negative thermal ion mass spectrometry of osmium, rhenium and iridium: Geochimica et Cosmochimica Acta, v. 55, p. 397–401, doi:10.1016/0016-7037(91)90427-7.

Davis, G.H., and Bump, A.P., 2009, Structural geologic evolution of the Colorado Plateau, *in* Kay, S.M., Ramos, V.A., and Dickinson, W.R. eds., Backbone of the Americas: Shallow Subduction, Plateau Uplift, and Ridge and Terrane Collision, Geological Society of America, doi:10.1130/2009.1204(05).

Dickinson, W.R., Klute, M.A., Hayes, M.J., Janecke, S.U., Lundin, E.R., McKITTRICK, M.A., and Olivares, M.D., 1988, Paleogeographic and paleotectonic setting of Laramide sedimentary basins in the central Rocky Mountain region: GSA Bulletin, v. 100, p. 1023–1039, doi:10.1130/0016-7606(1988)100<1023:PAPSOL>2.3.CO;2.

Doebelin, N., and Kleeberg, R., 2015, Profex: a graphical user interface for the Rietveld refinement program BGMN: Journal of Applied Crystallography, v. 48, p. 1573–1580, doi:10.1107/S1600576715014685.

Doelling, H.H., 2002, Geologic map of the Moab and eastern part of the San Rafael Desert 30' x 60' quadrangles, Grand and Emery Counties, Utah, and Mesa County, Colorado. M-180dm. UGS. 1:100,000 scale.

Doelling, H.H., 2004, Geologic map of the La Sal 30' x 60' quadrangle, San Juan, Wayne, and Garfield Counties, Utah, and Montrose and San Miguel Counties, Colorado. M-205. UGS. 1:100,000 scale.

Dumitru, T.A., Duddy, I.R., and Green, P.F., 1994, Mesozoic-Cenozoic burial, uplift, and erosion history of the west-central Colorado Plateau: Geology, v. 22, p. 499–502, doi:10.1130/0091-7613(1994)022<0499:MCBUAE>2.3.CO;2.

Faure, Gunter., and Mensing, T.M., 2005, Isotopes: principles and applications.: Hoboken, N.J., Wiley, xxvii, 897 p.

Hemming, S.R., Hall, C.M., Biscaye, P.E., Higgins, S.M., Bond, G.C., McManus, J.F., Barber, D.C., Andrews, J.T., and Broecker, W.S., 2002, 40Arr39Ar ages and 40Ar) concentrations of fine-grained sediment fractions from North Atlantic Heinrich layers: , p. 21.

Hollingsworth, E.R., Ressel, M.W., and Henry, C.D., 2017, Age and Depth of Carlin-type Gold Deposits in the Southern Carlin Trend: Eocene Mountain Lakes, Big Volcanoes, and Widespread, Shallow Hydrothermal Circulation, *in* Bedell, R.L. and Ressel, M.W. eds., Shallow Expressions of Carlin-type Systems, Alligator Ridge and Emigrant Mines, Nevada: Geological Society of Nevada field trip guidebook, 64, p. 149–173.

Humphreys, E., 2009, Relation of flat subduction to magmatism and deformation in the western United States, *in* Backbone of the Americas: Shallow Subduction, Plateau Uplift, and Ridge and Terrane Collision, Geological Society of America, doi:10.1130/2009.1204(04).

Humphreys, E., Hessler, E., Dueker, K., Farmer, G.L., Erslev, E., and Atwater, T., 2003, How Laramide-Age Hydration of North American Lithosphere by the Farallon Slab Controlled Subsequent Activity in the Western United States: International Geology Review, v. 45, p. 575–595, doi:10.2747/0020-6814.45.7.575.

Lipman, P.W., Prostka, H.J., Christiansen, R.L., Sutton, J., Sabine, P.A., and Skelhorn, R.R., 1972, A Discussion on volcanism and the structure of the Earth - Cenozoic volcanism and plate-tectonic evolution of the Western United States. I. Early and middle cenozoic: Philosophical Transactions of the Royal Society of London. Series A, Mathematical and Physical Sciences, v. 271, p. 217–248, doi:10.1098/rsta.1972.0008.

Ludwig, K.R., 2012, User's Manual for Isoplot 3.75-4.14: A Geochronological Toolkit for Microsoft Excel: Berkeley Geochronology Center Special Publication, v. 5, p. 75.

McIntosh, J.C., and Ferguson, G., 2021, Deep Meteoric Water Circulation in Earth's Crust: Geophysical Research Letters, v. 48, p. e2020GL090461, doi:https://doi.org/10.1029/2020GL090461.

Morgan, J.W., and Walker, R.J., 1989, Isotopic determinations of rhenium and osmium in meteorites by using fusion, distillation and ion-exchange separations: Analytica Chimica Acta, v. 222, p. 291–300.

Murray, K.E., Reiners, P.W., and Thomson, S.N., 2016, Rapid Pliocene–Pleistocene erosion of the central Colorado Plateau documented by apatite thermochronology from the Henry Mountains: Geology, v. 44, p. 483–486, doi:10.1130/G37733.1.

Murray, K.E., Reiners, P.W., Thomson, S.N., Robert, X., and Whipple, K.X., 2019, The thermochronologic record of erosion and magmatism in the Canyonlands region of the Colorado Plateau: American Journal of Science, v. 319, p. 339–380, doi:10.2475/05.2019.01.

Nelson, S.T., Davidson, J.P., and Sullivan, K.R., 1992, New age determinations of central Colorado Plateau laccoliths, Utah: Recognizing disturbed K-Ar systematics and re-evaluating tectonomagmatic relationships: GSA Bulletin, v. 104, p. 1547–1560, doi:10.1130/0016-7606(1992)104<1547:NADOCC>2.3.CO;2.

Nuccio, V.F., and Condon, S.M., 1996, Burial and Thermal History of the Paradox Basin, Utah and Colorado, and Petroleum Potential of the Middle Pennsylvanian Paradox Formation: U.S. Geological Survey Bulletin 2000-O, p. 40.

Pevear, D.R., 1999, Illite and hydrocarbon exploration: Proceedings of the National Academy of Sciences, v. 96, p. 3440–3446, doi:10.1073/pnas.96.7.3440.

Rasmussen, L., and Rasmussen, D.L., 2009, Burial History Analysis of the Pennsylvanian Petroleum System in the Deep Paradox Basin Fold and Fault Belt, Colorado and Utah: Rocky Mountain Association of Geologists Special Publication, p. 71.

Rosera, J.M., Gaynor, S.P., and Coleman, D.S., 2021, Spatio-Temporal Shifts in Magmatism and Mineralization in Northern Colorado Beginning in the Late Eocene: Economic Geology, v. 116, p. 987–1010, doi:10.5382/econgeo.4815.

Smoliar, M.I., Walker, R.J., and Morgan, J.W., 1996, Re-Os Ages of Group IIA, IIIA, IVA, and IVB Iron Meteorites: Science, v. 271, p. 1099–1102, doi:10.1126/science.271.5252.1099.

Thirumalai, K., Singh, A., and Ramesh, R., 2011, A MATLAB Code to Perform Weighted Linear Regression with (correlated or uncorrelated) Errors in Bivariate Data: Journal of the Geological Society of India, v. 77, p. 377–380.

Tindall, S.E., Storm, L.P., Jenesky, T.A., and Simpson, E.L., 2010, Growth faults in the Kaiparowits Basin, Utah, pinpoint initial Laramide deformation in the western Colorado Plateau: Lithosphere, v. 2, p. 221–231, doi:10.1130/L79.1.

Villa, I.M., De Bièvre, P., Holden, N.E., and Renne, P.R., 2015, IUPAC-IUGS recommendation on the half life of 87Rb: Geochimica et Cosmochimica Acta, v. 164, p. 382–385, doi:10.1016/j.gca.2015.05.025.

Withington, C. F., 1955, Geologic Map of the Paradox Quadrangle, Colorado, Map GQ 72, USGS.

Ylagan, R.F., Kim, C.S., Pevear, D.R., and Vrolijk, P.J., 2002, Illite polytype quantification for accurate K-Ar age determination: American Mineralogist, v. 87, p. 1536–1545, doi:10.2138/am-2002-11-1203.